On the dynamics and modelling of a micro electro-mechanical structure (MEMS)

I. Bucher[1], A. Elka[1] and E. Balmes[2]

[1]Dynamics Laboratory,
Faculty of Mechanical Engineering
Technion, Haifa 32000, Israel
e-mail: bucher@technion.ac.il

[2]MSSMat,
Ecole Centrale Paris,
92295 Chatenay Malabry Cedex, France
e-mail: balmes@mss.ecp.fr

Abstract

This paper describes a numerically efficient modelling procedure that couples a dynamic-elastic model of a miniature rate gyroscope to an electrostatic force-field. Alongside the numerical modelling, an experimental system is presented where a dynamical model consisting of operating deflection shapes, damping factors and response levels are obtained under a microscope. In the numerical part, a highly efficient software tool (SDT) enabled us to conveniently combine and manipulate a full-size finite-element model for the structure, with a custom numerical model of the electrostatic field in a manner that transient and steady-state behaviour as well as stability (pull-in) analysis could be performed.

This work follows the footsteps of traditional dynamic or modal testing to a point where some unique features existing in MEMS devices can be observed. Some of these phenomena were explained by a reconciliation of experimental and numerical data and internal resonance mechanism was identified.

1 Introduction

A variety of numerical methods and algorithms for the computation of electrostatic field problems of 3D geometries have been reported in the past [1].

However, most of these tools provide limited capabilities in terms transient dynamics modelling that has a sufficiently fast 3D computation scheme. The proposed approach although suitable for a special family of devices provides an ability to combine model generation and visualization of the distribution of the electrostatic force with a fast simulation of the coupled dynamics.

1.1 Rate gyro description

The device, often addressed as "a vibrating rate gyroscope" [4] was designed and built at the Technion [2] and it consists of a vibrating upper mass connected by a cantilever-beam to a rigid frame. The device is made of silicon by a bulk micro machining process. Two electrodes are deposited on the lower (stationary) and upper (vibrating mass) parts. Additionally, a VLSI electronic chip is placed on the lower part to perform the necessary actuation and signal processing tasks. There is a 7 micron spacing between the electrodes and the vibrating part has a proof mass which is 2x2mm having a thickness of 0.1 mm (100 micron). The proof mass is supported by the cantilever beam having a cross-section of 0.1x0.1 mm and which is 3mm long.

The structural part of the device is depicted in figure 1.

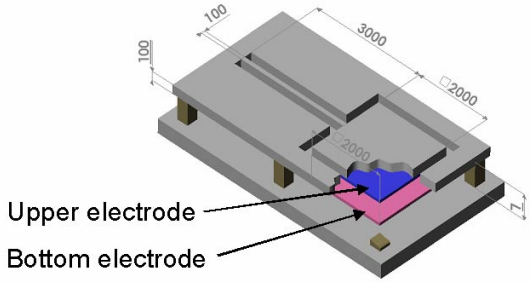

Figure 1: The gyro device – a CAD model

A cut through the structure is shown in figure 1 to expose the lower and upper electrodes.

1.2 Principle of operation

The device makes use of the Coriolis effect where a voltage potential is imposed across the electrodes (see figure 2) to generate an electrostatic force.

The externally imposed electrostatic field is operating here over a gap of 7 micro-meters to excite a specific vibration mode shape in the Y-direction (see fig. 2) while the rate of turn of these devices--Ω, creates, by means of a coupling Coriolis force

$$Fe_x = 2m\dot{Y}e_y \times \Omega e_z \qquad (1)$$

where e_x, e_y, e_z are unit vectors in the direction of the coordinate system in figure 2.

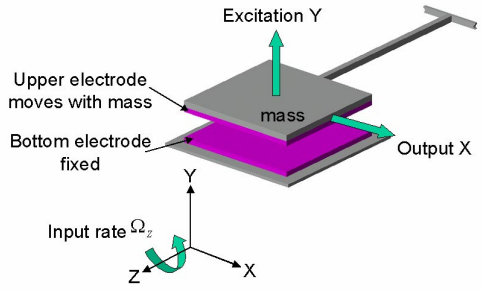

Figure 2: Principle of operation

Both modes, the excited and sensed ones, have close natural frequencies to allow for a sufficient sensitivity of the device, namely sufficiently large vibration levels in the *X* and *Y* directions. Equation 1 shows that sensed mode develops a deflection serving as a direct indication for the rate of turn, Ω.

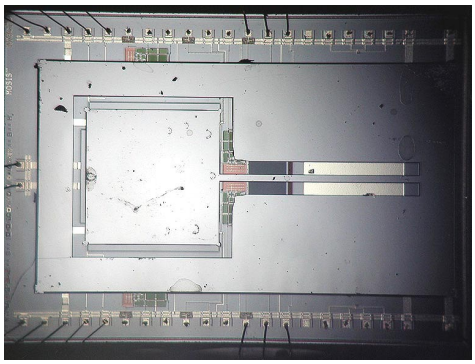

Figure 3: Top view of the device under a microscope

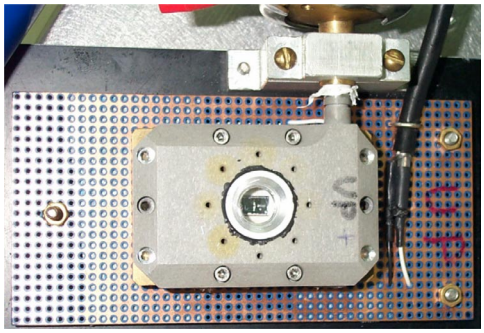

Figure 4: Top view of the device under a microscope

Figure 3 shows a photograph of the device where the proof-mass, the cantilever beam and a part of the electronics can be clearly observed. Figure 4 provide a broader view of the enclosure providing the required vacuum level. The sensor can observed through the sapphire window in the middle.

The overall behaviour of the sensor evidently depends on several physical factors that need to be compared with the numerical model. Indeed, in our experiment, it was found that several parameters, in particular, mass and stiffness, much like in full scale structure were important. Here, due to the small size, the damping of the squeezed air-film and some unexpected cross coupling effects caused by the electrostatic field, were observed.

Fully coupled analysis of the 3D electric potential and the resulting electrostatic force which is coupled to the vibration of the device require a heavy computational load. In fact such a simulation may last for many hours or even more for a full transient analysis. For this reason, we have used in this work an efficient modelling procedure making use of the small gap between the electrodes.

2 Theoretical background

This section outlines the theory and the assumptions behind the numerical model that was developed.

2.1 The structural part

The structural part consists of a material-anisotropic finite-element model imported from Ansys™ into Matlab™ by using SDT ([3]). The software utility allowed us to import the mass and stiffness matrices as well as the complete geometry of the structure that was used in the custom electrostatic model.

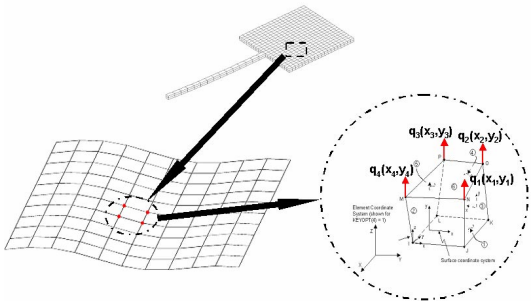

Figure 5: FE-mesh on the upper electrode

As can be seen in right hand side of figure 5, each element had 3 DOFs for each of the 8 nodes and the isotropic material properties that provided nearly identical results to the anisotropic properties are provided in Table 1.

Material	Density Kg/micron^3	Young's Modulus microNewtons/micron^2	Poisson's Ratio	Free-space permittivity microNewtons/Volt^2	Element type
Si (100)	2330e-18	131e3	0.064	8.852e-6	Solid 45

Table 1: Mechanical properties of silicon

2.2 The electric part

In this section we derive a closed form expression for the generalised electrostatic forces acting at the nodes. For this purpose, the electric potential energy that is contained in the volume between the electrodes is expressed as:

$$U_E = \frac{1}{2}\int_v D \cdot E dV \qquad (2)$$

When $D = \varepsilon E$ [6] is substituted, it is possible to express the total potential energy as a function of the electric field, *E*.

$$U_E = \frac{1}{2}\int_v \varepsilon E^2 dv \qquad (3)$$

Having defined the mechanical degrees of freedom we are able to obtain an expression for the electrostatic force:

$$g_i = -\frac{\partial U_e}{\partial q_i}, \qquad i = 1 \ldots n \qquad (4)$$

Here g_i is the generalised force that is related to the q_i mechanical degree of freedom.

The electric field is created by a potential difference, $V(t)$ across the electrodes, due to this voltage, an electrostatic force is developed. This force operates over a gap (between the top and bottom electrodes) that remains much smaller than its width and length. Under this assumption (see [6,7]) it is assumed that the total potential energy in equation 2, can be computed by integration on the volume which is contained only between the electrodes. This assumption practically means that any fringing effects of the electric field are neglected and the computation procedure is thus greatly simplified.

The volume over which the integration of equation 2 is performed changes with the deformation of the upper electrode; therefore the surface of the FE grid is being used for the computation of the electrostatic force.

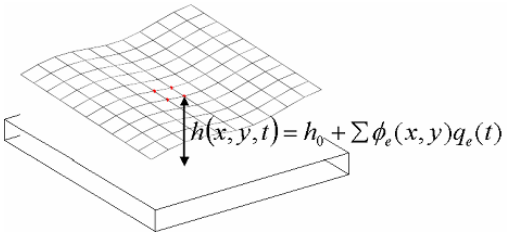

Figure 6: Air gap between the electrodes under a deformed state

From equation (3) we can obtain an expression for the electric potential energy where a volume element can be expressed as $h\,dx\,dy$ leading to:

$$U_E = \varepsilon \frac{V^2}{2}\int_A \frac{dx\,dy}{h(x,y,t)} \qquad (5)$$

Here $h(x,y,t)$ is the air gap between the electrodes as shown in figure (2). The gap can be directly expressed using the structural shape functions of the k^{th} element:

$$h_k(x,y,t) = h_0 + \sum_i {}_k\phi_i(x,y) q_i(t) \qquad (6)$$

Where h_0 - the initial gap between electrodes, ${}_k\phi_i$ - structural shape function, q_i - structural DOF.

The generalized electrostatic force can be expressed using equation 4, as

$$g_k(t) = \varepsilon \frac{V^2}{2}\sum_i \int_A \frac{{}_k\phi_i(x,y)\,dxdy}{h^2(x,y,t)} \qquad (7)$$

Here, the summation is around a single node of the contribution of all surrounding elements (see fig. 7)

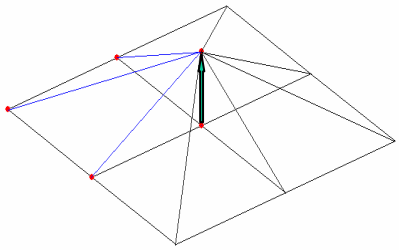

Figure 7: Electrode's deformation due to a virtual motion of the k^{th} DOF

An efficient method for a numerical evaluation of the electrostatic force is required and for this reason, a semi-analytical-numerical integration scheme is introduced.

The structural shape functions on the electrode can be computed by (as shown in fig. 5) the relation between unit displacement and coefficients, Figure 3.

$$ {}_k\phi_i(x,y) = \begin{pmatrix} 1 & x & y & xy \end{pmatrix} \begin{pmatrix} \beta_{1i} \\ \beta_{2i} \\ \beta_{3i} \\ \beta_{4i} \end{pmatrix} \tag{8} $$

For each element, we have (x_n, y_n), $n = 1 \ldots 4$, and the shape function can be computed after solving:

$$ \begin{bmatrix} 1 & x_1 & y_1 & x_1 y_1 \\ 1 & x_2 & y_2 & x_2 y_2 \\ 1 & x_3 & y_3 & x_3 y_3 \\ 1 & x_4 & y_4 & x_4 y_4 \end{bmatrix} \begin{pmatrix} \beta_{1i} \\ \beta_{2i} \\ \beta_{3i} \\ \beta_{4i} \end{pmatrix} = \begin{bmatrix} 1 \\ 0 \\ 0 \\ 0 \end{bmatrix} \tag{9} $$

The generalised force is computed at every time-step by means of a Guassian-quadrature approximating the expression in equation 10.

$$ g_k(t) = \varepsilon \frac{V^2}{2} \sum_i \int_{y_{\min}}^{y_{\max}} \int_{x_{\min}}^{x_{\max}} \frac{{}_k\phi_i(x,y)\, dx dy}{\left(h_0 + {}_k\phi_i(x,y) q_i(t)\right)^2} \tag{10} $$

It is worthy of mentioning that the expression for the nodal electrostatic force, depends on the generalised displacements $q_k(t)$ and thus is a function of the mechanical deformation state.

2.3 Model order reduction and scaling

The speed of execution and the appropriate scaling of the parameters are important factors in the transient analysis. Efficiency is essential in particular in light of the fact that equation 10 has to be computed at every time-step. Greater efficiency is achieved by a applying a scaling procedure to the parameters followed by an order reduction scheme converting a model with typically several thousands degrees to 10 DOFs.

A numerical model-order reduction scheme, leads to the form

$$ M\ddot{q} + C\dot{q} + Kq = g(q,V) \tag{11} $$

where M, C, K are the mass, damping and stiffness matrices while q is the vector of DOFs (typically several thousands). $g(q,V)$ stands for the electrostatic force and V is the externally applied voltage.

The order reduction scheme follows two stages where in the first stage a standard Craig-Bampton approach [5] is taken while the following step applies a balancing transformation [8]. The balancing transformation has improved the numerical conditioning considerably while detecting non-controllable (thus non-affecting) degrees of freedom.

The scaling procedure acts by defining new state variables and a new time scale

$$ Q(T) = \frac{q(T)}{h_0}, \quad T = \omega t \tag{12} $$

where ω is a reference frequency, leading to

$$ \ddot{Q} + \frac{M^{-1}C}{\omega}\dot{Q} + \frac{M^{-1}K}{\omega^2} Y = \frac{M^{-1} g\left(Q, V\left(T/\omega\right)\right)}{h_0 \omega^2} \tag{13} $$

where here $\dot{Q} = \frac{dQ}{dT}$ $\ddot{Q} = \frac{d^2Q}{dT^2}$.

The new system has natural frequencies that are scaled down by ω allowing the integration algorithm to take large time steps compared with the original time scaling.

2.4 Coupled model computational scheme

The computational scheme can be visualised by the block diagram in figure 8. In this figure the linkage between the structural and the electrostatic part is highlighted. Indeed, for every (newly obtained) deformation state, a new distribution of the electrostatic force must be recomputed.

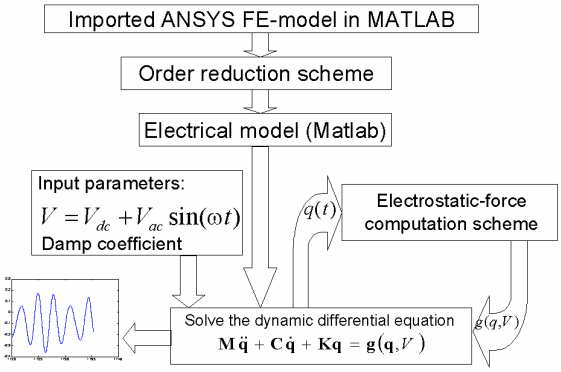

Figure 8 Computational scheme

The nonlinear nature of the coupling effect and the electrostatic force distribution (computed with equation 10), is demonstrated in figure 9. In this figure, 3 formation states belonging to 3 different modeshapes are shown. For each modeshape, the matching electrostatic force distribution (as computed by equation 10) is shown.

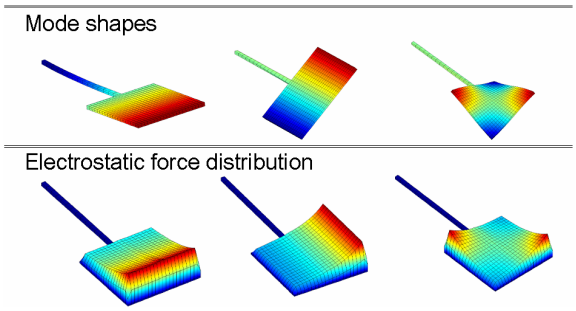

Figure 9: Mode shapes and Electrostatic force distribution

Figure 9 demonstrates the nonlinear dependency of the electrostatic force magnitude on the local air-gap.

3 Experimental work

The laboratory set-up is schematically depicted in figure 10.

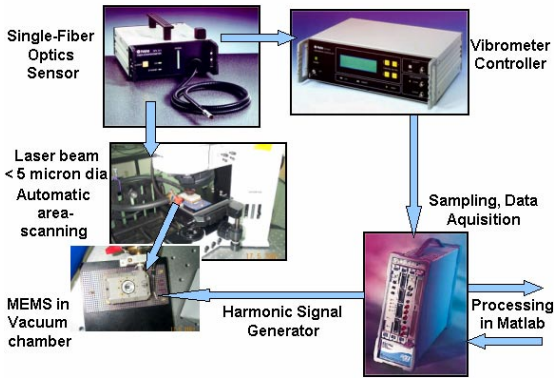

Figure 10 Laboratory set-up

In this set-up, a computer controlled excitation voltage is being used to excite vibrations in the device while it is contained in a vacuum preserving enclosure. The device was placed under a microscope equipped with a scanning laser sensor. The vacuum level in the enclosure (see fig. 4), was controlled by an external vacuum pump and monitored by a special gauge.

A parametric study was carried out and the results are depicted below.

Firstly the effect of DC and AC voltage levels was examined. It is a well known phenomenon in electrodynamics that the DC and AC amplitudes affect the dynamics of such devices, but is worthy of an experimental study since this effect is difficult to quantify with a great precision when replying on a model. The precision of the device, which is used as a sensor, depends to a great extent on a successful calibration and characterisation.

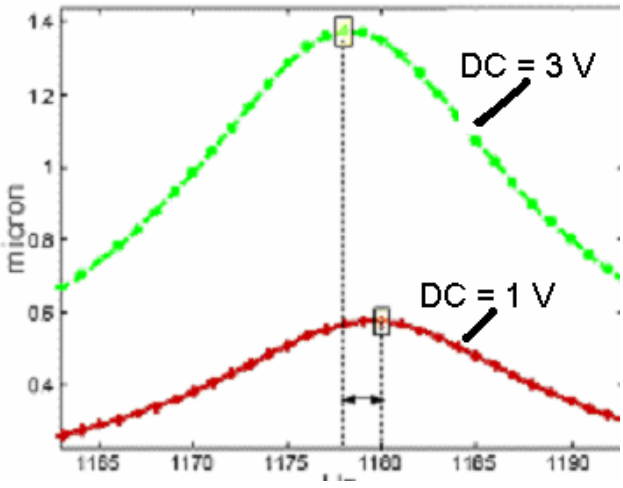

Figure 11 Response 1st harmonic under V_{dc}=1,3 [V]

Indeed, figure 11 shows that in addition to obtaining larger response amplitude, higher DC-voltage shifts the average resonance frequency by about 2 Hz. This fact can be explained by

examination of equation 7. When an input voltage of the form

$$V = V_{dc} + V_{ac}\sin\omega t \qquad (14)$$

is being used, the force is proportional to

$$V^2 = V_{dc}^{\ 2} + \frac{1}{2}V_{ac}^2 + 2V_{dc}V_{ac}\sin\omega t - \frac{1}{2}V_{ac}^2\cos 2\omega t \quad (15)$$

It can be seen that the amplitude of the first harmonic of the force is directly proportional to V_{dc}.

The change in the natural frequency can be explained by considering a simplified model of the electrostatic actuator in the form of a parallel-plates capacitor. In this device, the force behaves according to $F_N = -\frac{\varepsilon A V^2}{2(h_0 + y)^2}$, or

$$F_N \approx -\frac{\varepsilon A V^2}{2h_0^2} + \frac{\varepsilon A V^2}{h_0^3} y \qquad (15)$$

The second term in equation 15, behaves like a negative stiffness term thus having a softening effect.

A similar effect is achieved when the AC voltage is increased.

The effect of vacuum level on the damping appears in figure 12. Here, the increase in pressure, adds air that serves as spring and damper simultaneously, indeed larger pressure stiffens the devices and an increases in the resonance frequency can be observed. Damping can be seen to increase under a larger pressure. Indeed pressure elevation causes a decrease in response amplitude.

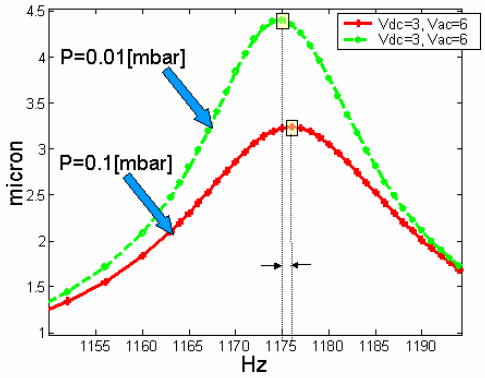

Figure 12 Effect of pressure level

An anomaly compared with ordinary structures is that the effective excitation force and the response are characterised for this device by means of several harmonics. A numerical study, showed us that the response can be modelled as a Fourier series of the form:

$$y = \left(\sum_{i=1}^{n} H_i \cos\left(i\omega t + \theta_i\right)\right) + \text{Residual} \qquad (16)$$

For an excitation voltage with a single harmonic (as in equation 14), we have measured;

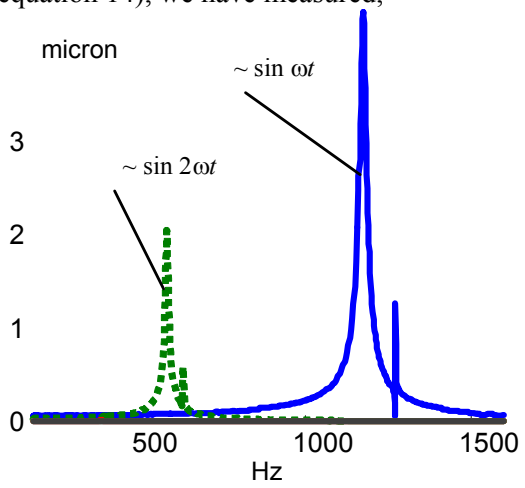

Figure 13 Decomposition of the measured response into harmonics

The second harmonic in figure 13, seem to have been excited at half the first natural frequency of the device which behaves in a linear manner by itself. Indeed the harmonic content of the response was investigated for the entire frequency range of interest and a typical output under an excitation of 585Hz is analysed in figure 14.

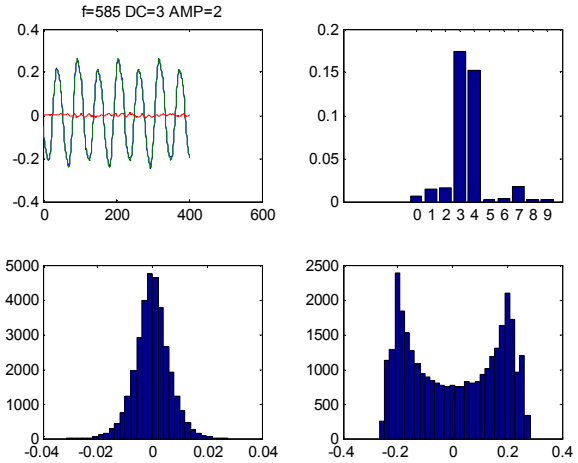

Figure 14 **Top left**: The measured, the fitted response and the residual. **Top right**: relative amplitudes of the various harmonics. **Bottom left**: amplitude distribution of the residual. **Bottom right**: Amplitude distribution of the response.

Figure 14 shows that the Fourier series model provides a good fit to the measured response. This fact is being strengthened by the probably distribution function of the residual that seems to posses a Guassian character. The top right plot

shows that not only the DC (0^{th} harmonic) and the first two harmonics participate, but also the 3^{rd} and 4^{th} harmonics are dominate at the specific operating frequency. This is contrary to the capacitor-like lumped model often used in the context of MEMS.

The response amplitude distribution (shown on the lower right of fig. 14), is typical for sinusoidal signals with slight asymmetry that can be attributed to the asymmetric nature of the electrostatic force.

3.1 Comparison with simulations

Comparisons of the measured response with two models were conducted. The models consisted of the above-mentioned finite-element model (having initially 1400 DOFs that were reduced to 10) and a simplified model for the lower modes treating the devices a as a two DOF structure.

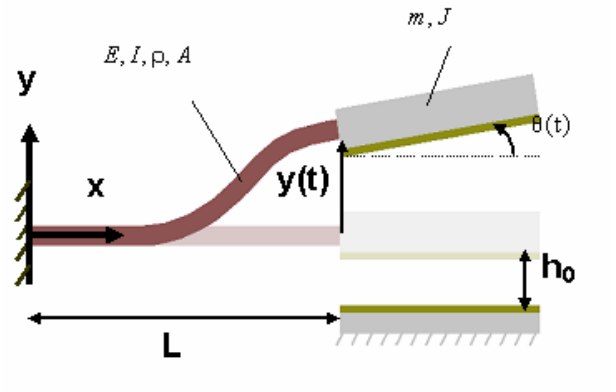

Figure 15: Two DOF model of the device

The simulated response for this case, showed a good fit in terms of frequency and some inaccuracy in the predicted response-amplitude that was attributed to residual charge effects on the electrodes.

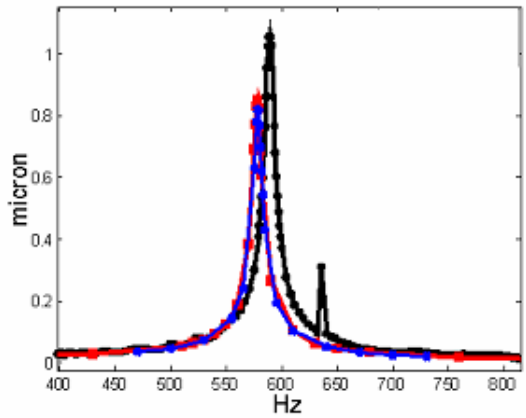

Figure 16: Comparison of a two DOF model, the finite element model and the measured response (2^{nd} harmonic) under V_{dc}=0 [V], V_{ac}=6 [V], pressure of P=0.01[mbar]. No 1^{st} harmonic was present in this case.

The measured response showed an additional 'spike' that corresponded to a vibration in the *x*-direction (see figure 2). This mode should not have been excited by the electrostatic force acting solely in the *y*-direction. An investigation of this phenomenon is described in the following section.

4 Internal resonance - model

A fine frequency scan (steps of 0.1 Hz) was conducted to allow for a verification of this 'spurious' peak.

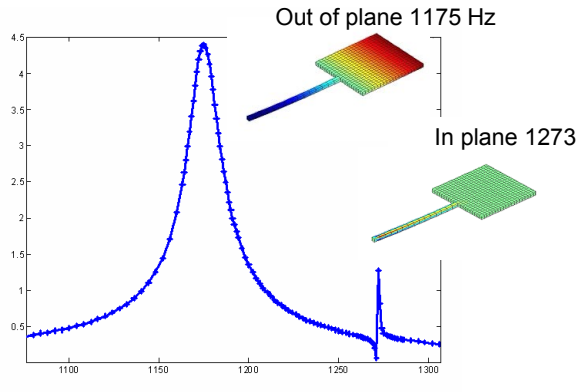

Figure 17: A fine frequency scan showing a sharp peak alongside with the main resonance.

The fact that this peak seemed repeatable and was characterised by very low damping, lead us to suspect that this peak was associate with a parallel motion of the electrodes. In this case, no squeeze-effect is generated and the damping is expected to be much lower than for a flapping mode (see top left in figure 9). The sideways motion of the electrodes was modelled as two degrees of freedom system where the excitation model exhibiting a *y*-axis motion is orthogonal to the sensing mode that is in the *x*-direction. Coupling between these modes that should have close natural frequencies is due to the Curioilis force (see equation 1).

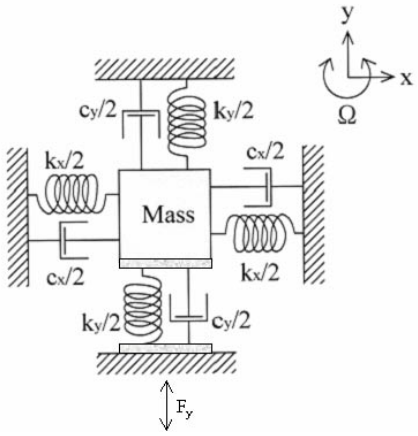

Figure 18: Two DOF model of the coupling

The equations of motion for this 2 DOF system models the two modes (see fig. 17):

$$\begin{aligned} &\ddot{x}+c\dot{x}-2\Omega\dot{y}+\left(\omega_x^2-\Omega^2\right)x=F_x \\ &\ddot{y}+c\dot{y}+2\Omega\dot{x}+\left(\omega_y^2-\Omega^2\right)y=F_y \end{aligned} \qquad (17)$$

Here ω_x, ω_y are the natural frequencies in the x and y directions respectively and F_x, F_y are the components of the electrostatic force. The electrostatic forces are approximated by assuming that there is a small deviation (x_0) from a fully parallel arrangement as is shown in figure 18.

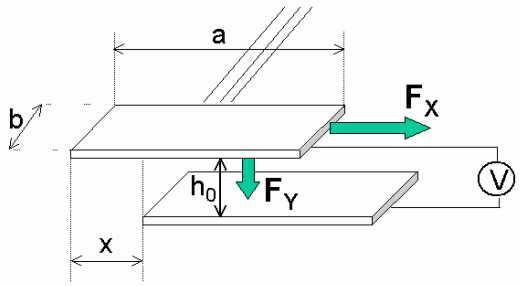

Figure 19: Electrostatic forces for the 2 DOF model

From standard electrostatics, it can be shown (e.g. [6]) that:

$$F_x=\frac{-sign(x+x_0)}{2}\frac{beV^2}{h_0+y} \qquad (18)$$

and the normal force:

$$F_y=-\frac{1}{2}\frac{\left(a-|x+x_0|\right)beV^2}{\left(h_0+y\right)^2} \qquad (19)$$

Assuming small deviations, we can develop the forces in a series to yield:

$$\begin{pmatrix}F_x\\F_y\end{pmatrix}=\begin{pmatrix}F_{x0}\\F_{y0}\end{pmatrix}-[\Delta K]\begin{pmatrix}x\\y\end{pmatrix} \qquad (20)$$

where we define a coupling matrix:

$$\Delta K=\frac{beV^2}{{h_0}^2}\begin{bmatrix}0 & \frac{1}{2}\\ \frac{1}{2} & \frac{(a-x_0)}{h_0}\end{bmatrix} \qquad (21)$$

Clearly the coupling matrix has coupling (off-diagonal) terms.

It can be seen in equation 15 that the term V^2, contains periodic components, thus we can deduce that some form of parametric excitation is present in this case. This periodicity introduces a modulation of the response that was indeed observed in the response measurements close to the 'peak's frequency.

4.1 Analysing the effect of the internal resonance

In order to asses how meaningful the internal resonance on the performance of the sensor, realistic damping estimates that were extracted in an experiment were used,

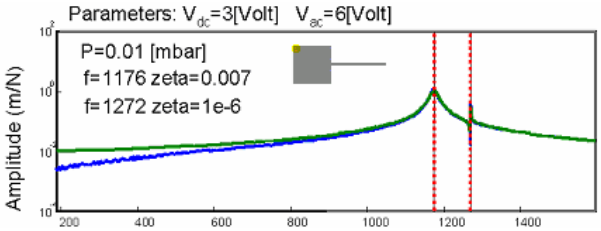

Figure 20 Curve-fitted response and the damping estimates

Having measured the typical response amplitudes in the *y*- direction we are able to use equation 17, and compare the relative contribution of the turn-rate compared with the internal resonance. Writing

$$\begin{aligned} &\ddot{x}_1+c\dot{x}_1+\left(\omega_x^2-\Omega^2\right)x_1=2\Omega\omega_y Y\cos\omega t \\ &\ddot{x}_2+c\dot{x}_2+\left(\omega_x^2-\Omega^2\right)x_2=F_x \end{aligned} \qquad (22)$$

we can estimate the steady-state amplitudes for an excitation of $V=3+6\sin\omega t\,[V]$ and for a small offset deviation of $x_0=0.2\mu m$. Note that the fitted damping levels were $\zeta_x=10^{-6}$, $\zeta_y=7\cdot10^{-3}$. For these parameters we compare $|x_2|/|x_1|$.

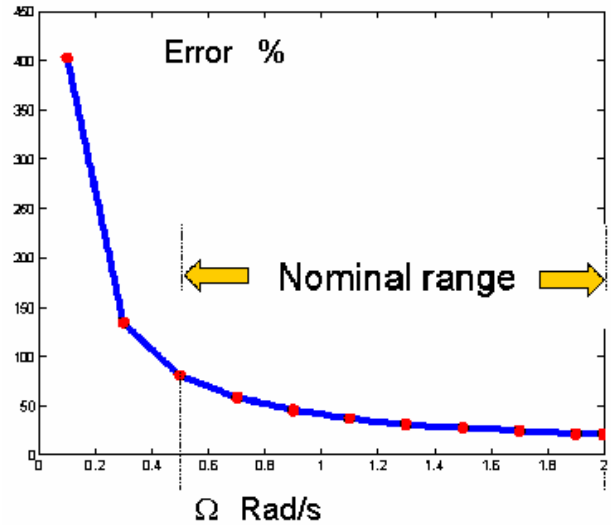

Figure 21: Sensor deviation Vs. turning rate

Figure 21, shows a surprisingly large deviation of the measured turning rate due to the mentioned phenomenon and the response due to cross-coupling is of a comparable size to the Coriolis effect.

5 Conclusions

The present paper discusses a modelling procedure of a MEMS device showing coupling between electrostatic and elastic effects. An efficient numerical scheme was presented and an experimental study was conducted. Good agreement was found between the modelled and measured response. The experimental procedure showed that an experimental calibration is essential for a reasonable prediction capability of the numerical model. Nevertheless it was proven that the experiments provide invaluable insight into the analytical and numerical models that allowed us to improve our physical understanding.

Acknowledgements

This work was supported by the Technion fund for the promotion of research.

References

[1] IEEE, Proceedings, The Ninth Annual International Workshop on Micro Electro Mechanical Systems, San Diego, California, USA (1996)

[2] O. Degani, Investigation of micro electromechanical systems incorporating modulated integrative differential optical sensing, M.Sc. thesis, Technion Israel, 1999

[3] E. Balmes, *Structural dynamics Toolbox for Matlab,* User guide V 4.1, (2002)

[4] M. H. Bao, *Handbook of Sensors and actuators*, Elsevier Amsterdam (200).

[5] R. J. Craig and M. Bampton, "Coupling of substructures for dynamic analyses", AIAA Journal,vol.6,no.7,pp.1313 –1319,1968.

[6] D. J. Griffiths, *Introduction to electrodynamics*, Prentice-hall, New-Jersey, 3rd ed. (1999).

[7] M. N. O. Sadiku, *Numerical techniques in electromagnetic*s, CRC press, Boca Raton, (1992)

[8] W. Gawronski, "Almost-Balanced Structural Dynamics", *Journal of Sound and Vibration* (1997) 202(5), pp. 669-687.